Supplementary information

Realistic atomic model for charge storage and charging dynamics of amorphous porous carbons

Table of Contents

Section 1. Gaussian random field model

In order to comprehend the newly developed Gaussian random field (GRF) in **Supplementary Section 2**, we summarized the content related to classical GRF method[1-4]. The GRF model is used to generate three-dimensional (3D) electrode matrix models of amorphous nanoporous carbons (consisting of pore voids and pore walls). The generation of the 3D electrode matrix model took statistical geometry parameters as input, and the statistical geometry parameters were obtained by fitting the experimental small angle X-ray scattering (SAXS) curve. The statistical geometry parameters are found related to the scattering peak that occurred in the experimental SAXS curve, as derived from the Teubner-Strey model[5].

Generating 3D electrode matrix models by GRF

We first demonstrate how the 3D electrode matrix model is generated. The 3D model showing a spatial coordinate $\mathbf{x}$ belonging to pore walls or pore voids follows the level-cut of GRF $y_{GRF}(\mathbf{x})$[1]:

$$\rho_{GRF}(\mathbf{x}) = \begin{cases} 1 & y_{GRF}(\mathbf{x}) < \alpha \\ 0 & y_{GRF}(\mathbf{x}) > \alpha \end{cases}, \tag{S1}$$

where $\rho_{GRF}(\mathbf{x}) = 1$ represents pore walls, and $\rho_{GRF}(\mathbf{x}) = 0$ refers to pore voids. The parameter α is determined by the pore void fraction ϵ_{void}, which satisfies[1]:

$$\mathrm{erf}\left(\frac{\alpha}{\sqrt{2}}\right) = 1 - 2\epsilon_{void}. \tag{S2}$$

$y_{GRF}(\mathbf{x})$ is constructed by[2]:

$$y_{GRF}(\mathbf{x}) = \sqrt{\frac{2}{M}} \sum_{i=1}^{M} \cos(\mathbf{k}_i \cdot \mathbf{x} - \psi_i), \tag{S3}$$

where the phase factor ψ_i distributes uniformly between 0 and 2π, and the M is the number of the cosine Gaussian wave, which is large enough to ensure a Gaussian distribution for $y_{GRF}(\mathbf{x})$. $\mathbf{k}_i$ is the wave vectors corresponding to the structure with a period of $\frac{2\pi}{|\mathbf{k}_i|}$ at the isotropically distributed direction. The module of the wave vector $|\mathbf{k}|$ follows the probability distribution $P(|\mathbf{k}|)$ of[2,3]:

$$P(|\mathbf{k}|) = \frac{2}{\pi}|\mathbf{k}| \int_0^\infty r g(r) \sin(|\mathbf{k}|r)\, \mathrm{d}r\,. \tag{S4}$$

$g(r)$ is the autocorrelation function of $y_{GRF}(\mathbf{x})$, defined as the orientational averaged correlation function of $y_{GRF}(\mathbf{x})$[3], $g(r) = \langle y_{GRF}(\mathbf{x}) y_{GRF}(\mathbf{x}+\mathbf{r})\rangle_{ori.\ av.}$, where the subscript $ori.\ av.$ represents orientational average of $\mathbf{r}$ vector with $|\mathbf{r}| = r$. To satisfy the periodic condition, $\mathbf{k}_i$ must be taken from the following sets[2]:

$$\mathbf{k}_i \in \left\{ \sum_{p=x,y,z} \frac{2\pi n_p}{\|\mathbf{e}_p\|^2} \mathbf{e}_p,\ \ n_p = 1, 2, 3, \ldots \right\}, \tag{S5}$$

where $\mathbf{e}_p$ represents for periodic box vectors. From Equations (S1)-(S5), it can be found that the 3D electrode matrix model is determined by the $g(r)$.

Getting autocorrelation function of GRF from experimental SAXS

In the Teubner-Strey model[5] that describes the scattering peaks in SAXS of periodic microstructures with two statistical geometry parameters l and ξ, the autocorrelation function of GRF $g(r)$ reads[2,5]:

$$g(r) = \frac{1}{\cosh\left(\frac{r}{\xi}\right)} \frac{\sin\left(\frac{2\pi r}{l}\right)}{\frac{2\pi r}{l}}, \tag{S6}$$

where the l represents the domain length corresponding to the periodicity of pore walls and pore voids, and ξ denotes the correlation length related to the association between neighbouring pores[2,3,5]. The two-point probability function $P_{11}(r)$, defined as the probability that two points with a distance of r belong to the same phase (pore wall or pore void) is[1,4]:

$$P_{11}(r) = \frac{1}{2\pi} \int_0^{g(r)} \frac{1}{\sqrt{1-t^2}} \left[\exp\left(-\frac{\alpha^2}{1+t} \right) \right] \mathrm{d}t + {\epsilon_{void}}^2, \tag{S7}$$

where the t is the dummy variable for integration. Then the intensity contribution by nanopores $I_{nanopores}$ with the scattering vectror q can be obtained as[2]:

$$I_{nanopores}(q) = K \int_0^\infty (P_{11}(r) - {\epsilon_{void}}^2) \frac{\sin(qr)}{qr} 4\pi r^2 \mathrm{d}r\,, \tag{S8}$$

where K is a constant related to the electron density difference between the two phases

(pore wall and pore void) and the scattering properties of electrons. Considering the scattering intensity from macroparticles obeying Porod's law $I_{macroparticles}(q) = q^{-a}$ (a is related to the shape of carbon particles, and is set to 4 in our case[6]) and the background C, the intensity of SAXS curve yields[2]:

$$I(q) = I_{nanopores}(q) + I_{macroparticles}(q) + C. \quad \text{(S9)}$$

Hence, the l and ξ can be obtained by fitting the experimental SAXS curve through Equations (S6)-(S9).

Position of the scattering peak determined by statistical geometry parameters

With statistical geometry parameters ξ and l determined, the position of the scattering peak q_{max} can be derived from the Teubner-Strey model[5]. In the Teubner-Strey model, the SAXS curve with a scattering peak situated at q_{max} follows a simpler form of[5]:

$$I(q) = \frac{I_0}{(1 - I_0/I_{max})(q^2/q_{max}^2 - 1)^2 + I_0/I_{max}}, \quad \text{(S10)}$$

where I_0 is related to the width of the peak, and I_{max} is the intensity of scattering peak position at q_{max}. Equation (S10) can be further simplified to the form of[5]:

$$I(q) = \frac{I_0}{a_2 + c_1 q^2 + c_2 q^4}. \quad \text{(S11)}$$

where the parameters follow $a_2 = 1$, $c_1 = \frac{-2(1-I_0/I_{max})}{q_{max}^2}$ and $c_2 = \frac{(1-I_0/I_{max})}{q_{max}^4}$. The statistical geometry parameters ξ and l follow[5]:

$$\xi = \left[\frac{1}{2}\left(\frac{a_2}{c_2}\right)^{\frac{1}{2}} + \frac{1}{4}\frac{c_1}{c_2}\right]^{-\frac{1}{2}}, \quad \text{(S12)}$$

$$l = 2\pi\left[\frac{1}{2}\left(\frac{a_2}{c_2}\right)^{\frac{1}{2}} - \frac{1}{4}\frac{c_1}{c_2}\right]^{-\frac{1}{2}}. \quad \text{(S13)}$$

Combining Equations (S10)-(S13), we obtained the relationship between statistical geometry parameters and the position of scattering peak q_{max} as:

$$q_{max} = \left[\left(\frac{2\pi}{l}\right)^2 - \frac{1}{\xi^2}\right]^{\frac{1}{2}}. \quad \text{(S14)}$$

Specifically, when $\frac{2\pi}{l} \leq \frac{1}{\xi}$, $I_0 \geq I_{max}$, the scattering peak will vanish (black line in **Supplementary Fig. 1**). The curve will have the Guinier behavior[7] ($I \sim exp(-q^2 R_g^2/3)$) or Debye-Anderson-Brumberger behaviour[8,9] ($I \sim 1/\left(6/R_g^2 + q^2\right)^2$) with the gyration radius R_g related to the average pore size[10].

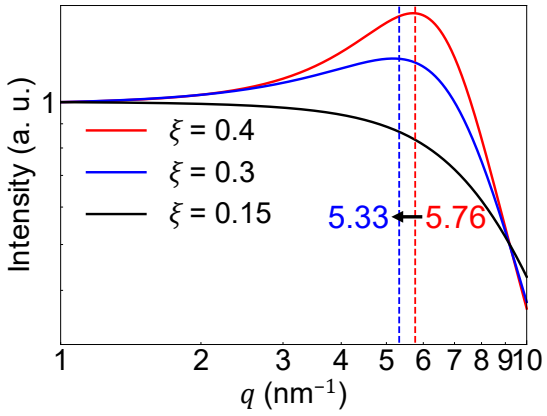

Supplementary Figure 1. Position of scattering peak. Comparison between the SAXS curve of GRF with $l = 1$ nm and ξ with different values. The dashed lines represent the peak position obtained by Equation (S14).

Section 2. Multiple scattering peaks GRF model

For porous carbon materials with multiple characteristic pore sizes, multiple scattering peaks in the SAXS curve can occur[11-13]. The cGRF applies a single set of ξ and l, which might bring incorrect values[14]. To address this, the multiple scattering peaks GRF (mGRF) model is proposed, which adopts the autocorrelation function $g_{mGRF}(r)$ of:

$$g_{mGRF}(r) = \sum_{i=1}^{N} a_i \frac{1}{\cosh\left(\frac{r}{\xi_i}\right)} \frac{\sin\left(\frac{2\pi r}{l_i}\right)}{\frac{2\pi r}{l_i}}, \quad \text{(S15)}$$

where each l_i represents the periodicity, ξ_i denotes the correlation or ordering between pores, and a_i is the weight of each scattering peak and is related to the surface area fraction. N_s is determined by the number of scattering peaks in the SAXS curve. By substituting the autocorrelation function $g_{mGRF}(r)$ into Equation (S7), the SAXS curve is fitted using Equations (S7)-(S9), getting the statistical geometry parameters l_i, ξ_i and a_i. The 3D electrode matrix model for mGRF $\rho_{mGRF}(\mathbf{x})$ is then generated through Equations (S1)-(S5).

For the experimental SAXS curve of the selected porous carbon, selections of N from 1 to 5 were tried, and the corresponding fitting results were compared to the experimental SAXS curve (**Supplementary Fig. 2a-b**). $N = 3, 4$ reach the maximum of the R^2, and they show identical autocorrelation functions (**Supplementary Fig. 2c**), leading to a similar 3D electrode matrix structure.

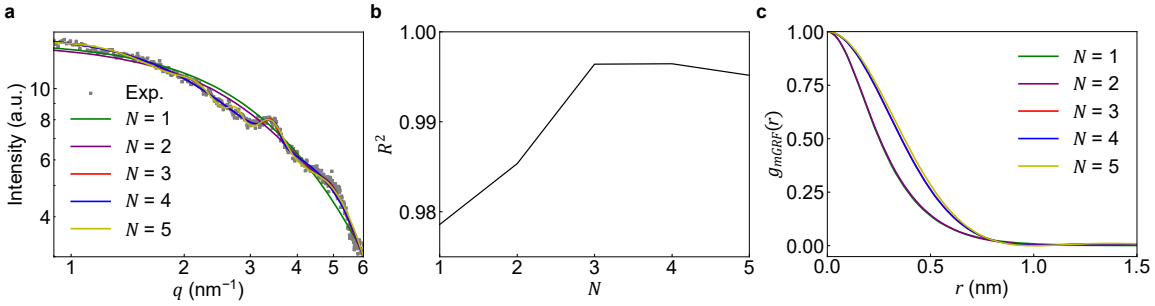

Supplementary Figure 2. Comparison among SAXS curves of mGRF with different *N*. a, SAXS curve of different *N*. **b**, The R^2 of mGRF with different *N*. **c**, The autocorrelation function of different *N*.

Section 3. Generation of atomic structure

After generating the 3D electrode matrix model by mGRF, which describes the pore wall as $\rho_{mGRF}(\mathbf{x}) = 1$ and conversely, the pore void as $\rho_{mGRF}(\mathbf{x}) = 0$, the atomic model is constructed by the hybrid 3D reverse molecular dynamics (H3D-RMD) method combining 3D reverse molecular dynamics with the reactive forcefield MD.

In H3D-RMD, the atomic model is denoted by a set of atoms at the position of $\{\mathbf{R}_i, i = 1, \dots, N_{atom}\}$. The 3D electrode matrix structure of the atomic model $\rho_{atom}(\mathbf{x})$ is defined as the spatial occupation of atoms, and each atom occupies a sphere with a van der Waals (vdW) radius r_{vdW}:

$$\rho_{atom}(\mathbf{x}) = u_c\left(r_{vdW} - \min_{\mathbf{R}_i}\{\|\mathbf{R}_i - \mathbf{x}\|\}\right), \tag{S16}$$

where u_c is the Heaviside step function. Therefore, $\rho_{atom}(\mathbf{x}) = 1$ represents the pore wall and $\rho_{atom}(\mathbf{x}) = 0$ represents the pore void. The structural difference between the atomic model and mGRF can be then defined as the squared error form:

$$\chi^2 = \frac{1}{V}\int_V [\rho_{atom}(\mathbf{x}) - \rho_{mGRF}(\mathbf{x})]^2 \mathrm{d}\mathbf{x}, \tag{S17}$$

where V is the box volume. To minimize the structural difference by the MD procedure, the error is written as the energy form of $U_m = \omega\chi^2$ by adding a hybridization rate ω with an energy unit. Simultaneously, the energy obtained by the reactive force field U_c should be considered to keep the atomic model with stable chemical structures. Hence the total energy of the atomic model U_t is:

$$U_t = U_m + U_c, \tag{S18}$$

and the force on the *i*th atom $\mathbf{F}_i$ is calculated as:

$$\mathbf{F}_i = -\frac{\partial U_t}{\partial \mathbf{R}_i}. \tag{S19}$$

The MD based on the force field in Equations (S18)-(S19) leads to minimizing χ^2 and stable chemical structure.

Section 4. Pore size characterized by the Voronoi sphere

The concept of the Voronoi sphere comes from the Voronoi diagram[15]. For a set of points representing the position of electrode atoms $\{\mathbf{R}_i, i = 1, \dots, N_{atom}\}$, the Voronoi diagram can be generated, in which each atom is surrounded by a Voronoi cell (**Supplementary Fig. 3a**). The Voronoi node $\mathbf{c}$ can be defined as the intersection of Voronoi cells. For $\{\mathbf{c}, \mathbf{R}_i, \mathbf{R}_j, \mathbf{R}_k, \mathbf{R}_l\} \subseteq \mathbb{R}^3$, the Voronoi node $\mathbf{c}$ satisfies:

$$|\mathbf{c} - \mathbf{R}_i| = |\mathbf{c} - \mathbf{R}_j| = |\mathbf{c} - \mathbf{R}_k| = |\mathbf{c} - \mathbf{R}_l|. \quad \text{(S20)}$$

Note that although the two-dimensional schematic in **Supplementary Fig. 3a** shows only three Voronoi cells intersecting at $\mathbf{c}$ for $\{\mathbf{c}, \mathbf{R}_i, \mathbf{R}_j, \mathbf{R}_k\} \subseteq \mathbb{R}^2$, the discussion of 3D space in Equation (S20) is not affected. When a sphere originating from Voronoi node $\mathbf{c}$ contacts with the vdW sphere of the corresponding electrode atoms $\mathbf{R}_i$, $\mathbf{R}_j$, $\mathbf{R}_k$, $\mathbf{R}_l$, the sphere is defined as the Voronoi sphere (dark grey spheres in **Supplementary Fig. 3b**). Thus, the radius of Voronoi sphere r_{voro} is defined as:

$$r_{voro} = \left(|\mathbf{c} - \mathbf{R}_{i,j,k,l}| - r_{vdW}\right). \quad \text{(S21)}$$

The diameter $d = 2r_{voro}$ is defined as the pore size. When the d is larger than the probing molecules (argon) with a diameter of 0.372 nm, the corresponding Voronoi node or Voronoi sphere marks the accessible pores (**Supplementary Fig. 3b**). Another advantage for the pores characterized by the Voronoi spheres and Voronoi nodes is that it also generates the accessible pore network (black lines in **Supplementary Fig. 3b**), which can be used to characterize pore length.

To validate the pore size measured by the Voronoi sphere, the diameter of the Voronoi sphere is compared with the pore size of the most widely used ideal pore models (nanoslit and nanotube) in **Supplementary Fig. 3c-d**.

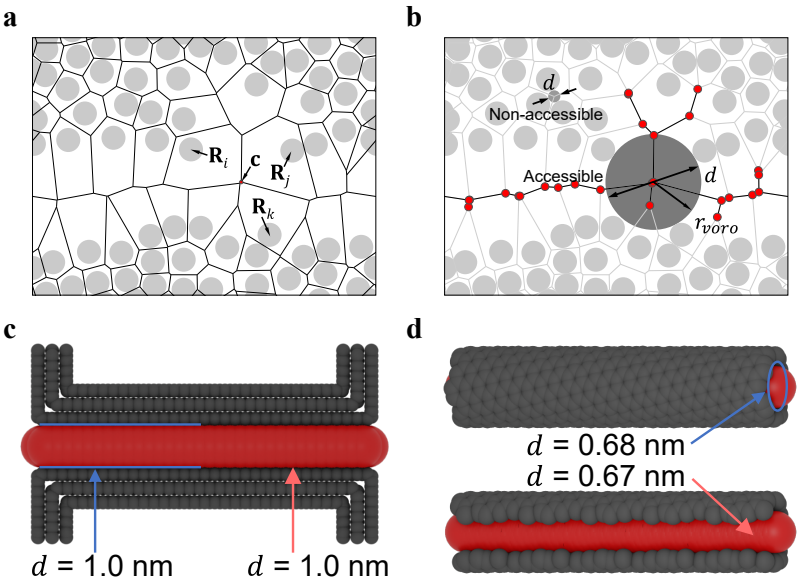

Supplementary Figure 3. The pore size measured by the Voronoi sphere. a, Voronoi diagram of a set of points. Lines in black form the Voronoi cells for each atom. One of the Voronoi node **c** is marked as a red point. **b**, Schematic of the Voronoi sphere. The red dots represent Voronoi nodes for accessible pores. The black lines represent the accessible pore network. **c**, Pore size of nanoslit compared with its Voronoi sphere. **d**, Pore size of nanotube compared with its Voronoi sphere.

Section 5. Local electrolyte structure extracted by Voronoi sphere

When n_i ions are included in the *i*th Voronoi sphere with a diameter of d and a volume of V_i, the number density for the specific pore size d is defined as:

$$\rho_{ion}(d) = \frac{\sum_i n_i}{\sum_i V_i}. \quad \text{(S22)}$$

Within a Voronoi sphere, we define the radial ion number density as the number density of the spherical shell between radii of $r - \Delta r$ and $r + \Delta r$ (Δr is the half step between sampling bins). When $n_{i,(r-\Delta r,r+\Delta r)}$ ions included in the spherical shell, whose volume is $V_{i,(r-\Delta r,r+\Delta r)}$, the radial ion number density is calculated as:

$$\rho_{ion}(d,r) = \frac{\sum_i n_{i,(r-\Delta r,r+\Delta r)}}{\sum_i V_{i,(r-\Delta r,r+\Delta r)}}. \quad \text{(S23)}$$

To evaluate the image charge effect and the capacitance for different-sized pores, the local electrode charge (LEC) is employed, which quantifies the charge of electrode atoms around adsorbed ions. For a single ion, LEC_{ion} is defined as the charges of electrode atoms within the coordination shell (the radius of the coordination shell is 0.63 nm[16]). The ensemble-averaged LEC is then computed by averaging LEC_{ion} values over all adsorbed ions residing in the Voronoi sphere with diameter d (the adsorbed ions are ions with electrode atoms coordinated with them).

To illustrate how the ion pair impacts the LEC, the ion separation and decoupling are evaluated. For a counter-ion in a Voronoi sphere with diameter d, the ion separation is defined as its distance to the nearest co-ion. The decoupling of counter-ion and co-ion pairs is assessed by the number of co-ions in coordination with counter-ions, given by the number of co-ions within a 0.77 nm radius coordination shell of counter-ions[16]. The smaller coordination number of counter-ion indicates that fewer co-ions are pairing with counter-ions, reflecting stronger decoupling of cation-anion pairs (**Supplementary Fig. 4c-d**).

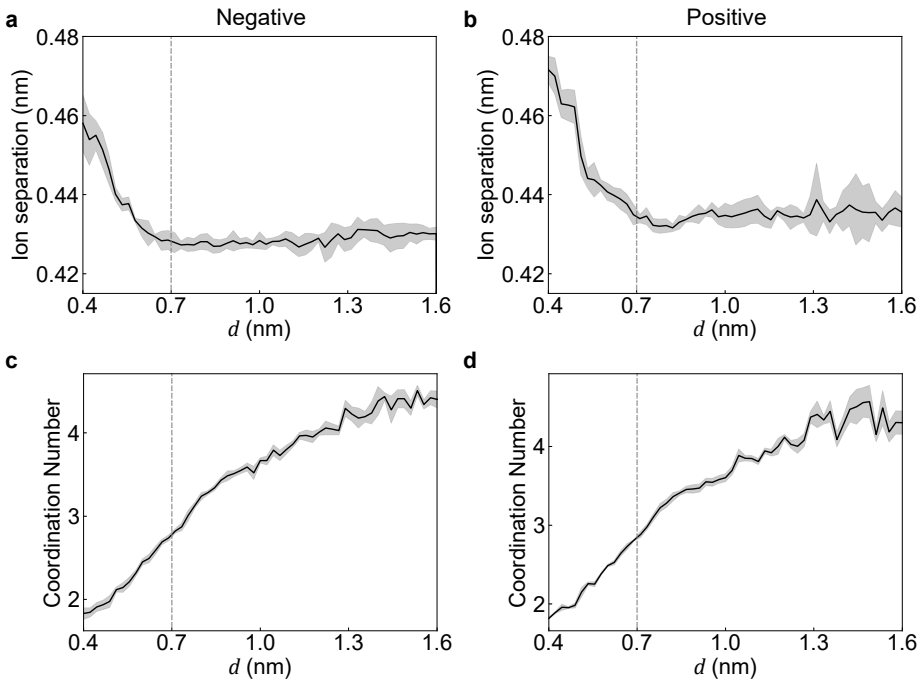

Supplementary Figure 4. The separation and decoupling of ion pairs. a,**b**, The separation between pairs of counter-ions and co-ions in negative (**a**) and positive (**b**) electrodes in different-sized pores. **c**,**d**, The decoupling of counter-ions and co-ions pairs evaluated by coordination number of counter-ions in negative (**c**) and positive (**d**) electrodes. The smaller coordination number corresponds to a stronger decoupling of cation-anion pairs.

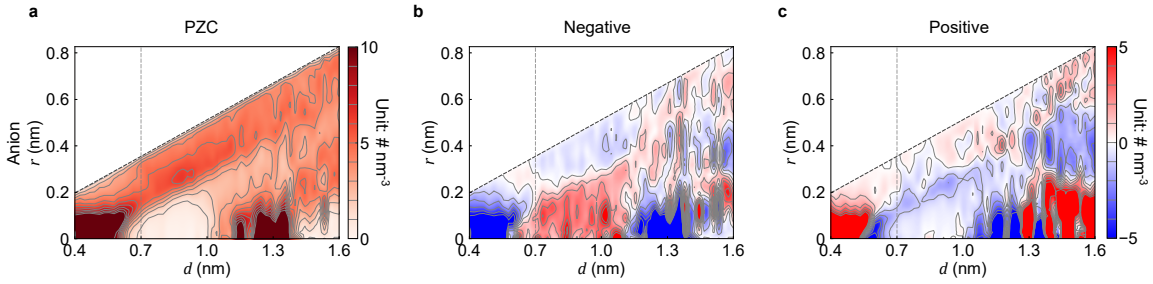

Supplementary Figure 5. The radial ion number density of anions. a, The radial ion number density of anions at the potential of zero charge (PZC). **b**,**c**, Change of radial ion number density of anions in negative (**b**) and positive (**c**) electrodes, compared with PZC.

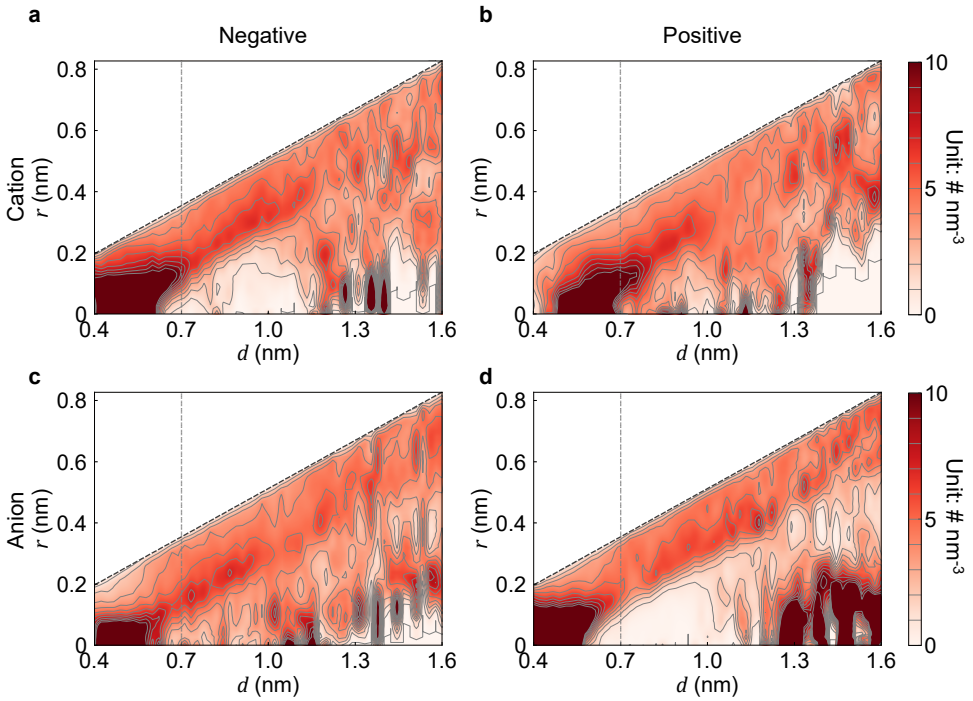

206

207 **Supplementary Figure 6. The radial ion number density. a**,**b**, Radial ion number
208 density of cations in negative (**a**) and positive (**b**) electrodes. **c**,**d**, Radial ion number
209 density of anions in negative (**c**) and positive (**d**) electrodes.

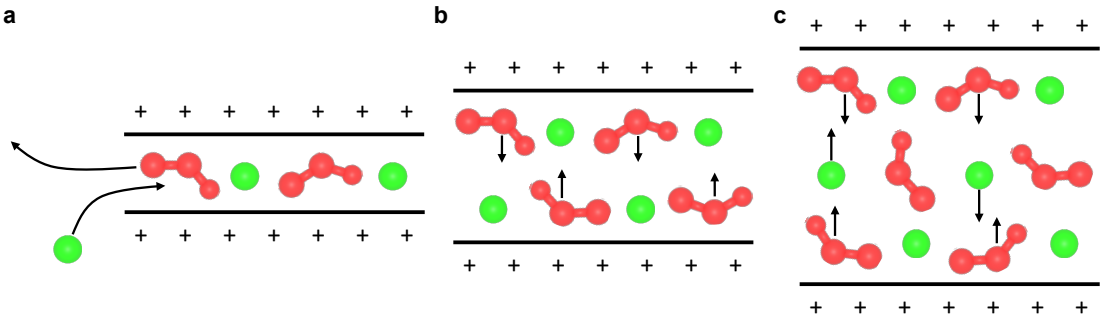

210

211 **Supplementary Figure 7. Schematics of charge storage process in different-sized**
212 **pores. a**, The ion exchange in ultramicropores. **b**,**c**, The ion transport between the pore
213 centre and pore wall in large micropores, when ions in the pore centre are almost
214 depleted (**b**) and another layer of ions in the pore centre is formed (**c**).

Section 6. The connectivity of ultramicropores

The ultramicropores are classified into deep and facial ultramicropores. The ultramicropore is defined as a deep ultramicropore when the Voronoi sphere of the ultramicropore doesn't overlap the Voronoi spheres representing large micropores (the distance between the Voronoi nodes is larger than the sum of Voronoi spheres' radii), due to these pores show elongated ion transport pathway. Conversely, the ultramicropore is defined as a facial ultramicropore when the Voronoi sphere overlaps the Voronoi sphere of large micropores, which means a direct connection between the ultramicropore and large micropores.

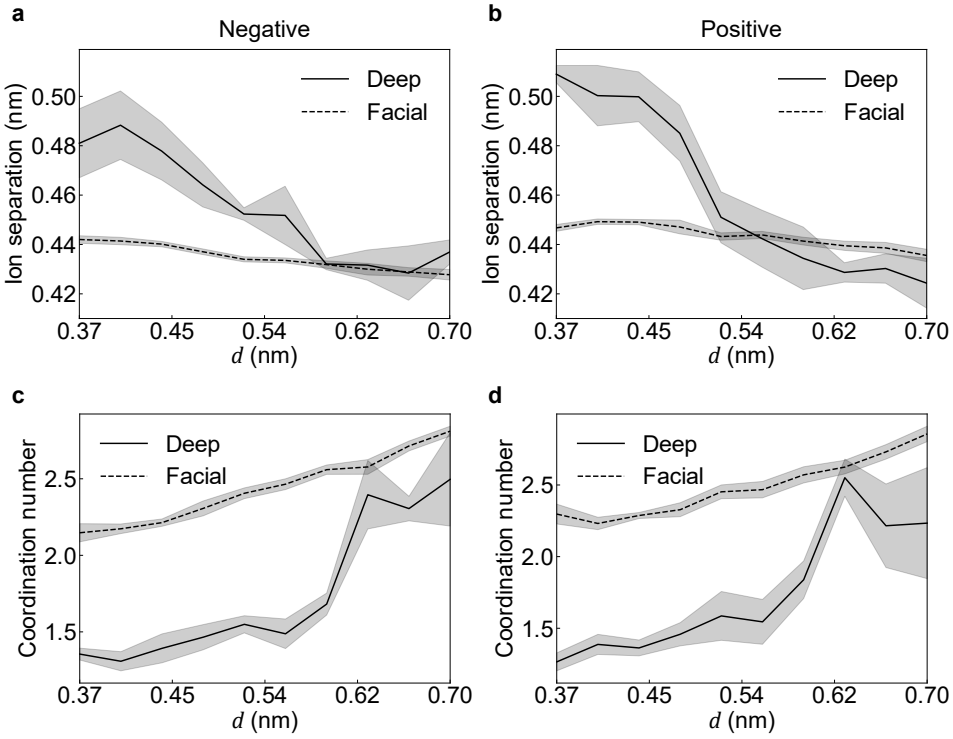

Supplementary Figure 8. The separation decoupling of ion pairs within different ultramicropores. a,**b**, The separation between pairs of counter-ions and co-ions in ultramicropores of negative (**a**) and positive (**b**) electrodes. **c**,**d**, The coordination number of counter-ions in ultramicropores of negative (**c**) and positive (**d**) electrodes, defined as the number of co-ions within the coordination shell.

Section 7. Fractal equivalent circuit

As shown in Fig. 4b of the main text, the simulated electrode is modeled by a fractal equivalent circuit (FEC), with 2 levels representing ion transport in ultramicropores and large micropores respectively. The impedance of level I circuit of Fig. 4b in the main text is:

$$Z_{\mathrm{I}} = \sqrt{R_{\mathrm{I}}}\sqrt{Z_{C_{\mathrm{I}}}}\coth\left[\frac{L_{\mathrm{I}}\sqrt{R_{\mathrm{I}}}}{\sqrt{Z_{C_{\mathrm{I}}}}}\right], \tag{S24}$$

where L_{I} is the pore length of ultramicropores, $R_{\mathrm{I}} = \frac{1}{\sigma_{\mathrm{I}}\pi r_{\mathrm{I}}^2}$ and $Z_{C_I} = \frac{1}{j\omega C_{\mathrm{I}} 2\pi r_{\mathrm{I}}}$ correspond to length-specific impedance by resistance and capacitance, respectively; σ_{I} is the ionic conductivity of ultramicropores, C_{I} is the area-specific capacitance of ultramicropores, r_{I} is the half-pore size of ultramicropores, and ω is the angle frequency.

The impedance of ultramicropores Z_{I} is parallel with the capacitance of large micropores (middle panel in Fig. 4b of main text), thus the impedance combining the capacitive impedance of large micropores and impedance of ultramicropores gives:

$$\frac{L_{\mathrm{II}}}{Z} = \frac{L_{\mathrm{II}}}{Z_{C_{\mathrm{II}}}} + \frac{n_{\mathrm{I}}}{Z_{\mathrm{I}}}, \tag{S25}$$

where L_{II} is the length of large micropores, n_{I} is the number of ultramicropores branching from the larger micropores, and $Z_{C_{\mathrm{II}}} = \frac{1}{(j\omega)^{\alpha} C_{\mathrm{II}} 2\pi r_{\mathrm{II}}}$ is the capacitive impedance of large micropores. The C_{II} refers to the area-specific capacitance of large micropores, r_{II} is the half pore size of large micropores, and α quantifies the CPE behaviour of the electrode caused by the distribution of pore size[17]. The impedance of the whole FEC shown in the middle panel of Fig. 4b of the main text is then calculated as:

$$Z_{FEC} = \sqrt{R_{\mathrm{II}}}\sqrt{Z}\coth\left[\frac{L_{\mathrm{II}}\sqrt{R_{\mathrm{II}}}}{\sqrt{Z}}\right], \tag{S26}$$

where $R_{\mathrm{II}} = \frac{1}{\sigma_{\mathrm{II}}\pi r_{\mathrm{II}}^2}$ is the length-specific resistance determined by the in-pore ionic

conductivity σ_{II}. Combining Equations (S24)-(S26), the impedance of the FEC can be written as:

$$Z_{FEC}(\omega) = \sqrt{R_{\mathrm{II}} \frac{L_{\mathrm{II}}\sqrt{R_{\mathrm{I}}}\coth\left[L_{\mathrm{I}}\sqrt{R_{\mathrm{I}}(j\omega)^{\alpha}C_{\mathrm{I}}2\pi r_{\mathrm{I}}}\right]}{n_{\mathrm{I}}\sqrt{(j\omega)^{\alpha}C_{\mathrm{I}}2\pi r_{\mathrm{I}}} + \sqrt{R_{\mathrm{I}}}(j\omega)^{\alpha}C_{\mathrm{II}}2\pi r_{\mathrm{II}}L_{\mathrm{II}}\coth\left[L_{\mathrm{I}}\sqrt{R_{\mathrm{I}}(j\omega)^{\alpha}C_{\mathrm{I}}2\pi r_{\mathrm{I}}}\right]}}}$$

$$\coth\left[L_{\mathrm{II}}\sqrt{R_{\mathrm{II}}\frac{n_{\mathrm{I}}\sqrt{(j\omega)^{\alpha}C_{\mathrm{I}}2\pi r_{\mathrm{I}}} + \sqrt{R_{\mathrm{I}}}(j\omega)^{\alpha}C_{\mathrm{II}}2\pi r_{\mathrm{II}}L_{\mathrm{II}}\coth\left[L_{\mathrm{I}}\sqrt{R_{\mathrm{I}}(j\omega)^{\alpha}C_{\mathrm{I}}2\pi r_{\mathrm{I}}}\right]}{L_{\mathrm{II}}\sqrt{R_{\mathrm{I}}}\coth\left[L_{\mathrm{I}}\sqrt{R_{\mathrm{I}}(j\omega)^{\alpha}C_{\mathrm{I}}2\pi r_{\mathrm{I}}}\right]}}\right]. \quad \text{(S27)}$$

Moreover, we discuss how the geometry parameters are obtained from the constructed electrode model. r_{I} and r_{II} are the average half-pore size given directly from the partition of ultramicropores and large micropores. The pore length is defined as the length of the shortest ion path connecting two ends of the pore through the pore centre (Fig. 4b in the main text). In practice, the pore network is employed (**Supplementary Fig. 3b**), ensuring that the ion path goes through the pore centre without overlapping electrode atoms[15]. After determining r_{I}, r_{II}, L_{I} and L_{II}, the n_{I} could be determined by matching SSA.

Supplementary Table 1. The geometry parameters from the atomic model

Geometry parameters	Value
r_{I}	0.25 nm
r_{II}	0.65 nm
Box size	6.00 nm
L_{I}	2.85 nm
n_{I}	5
L_{II}	7.46 nm

Supplementary Table 2. Capacitance and ionic conductivity for FEC to fit the charging process of the simulation.

Ultramicropores		Large micropores	
C_{I}	σ_{I}	C_{II}	σ_{II}
6.01 μF cm^{-2}	3.90×10^{-2} S m^{-1}	4.45 μF cm^{-2}	2.33×10^{-1} S m^{-1}

Section 8. Charging dynamics of nanoporous carbon

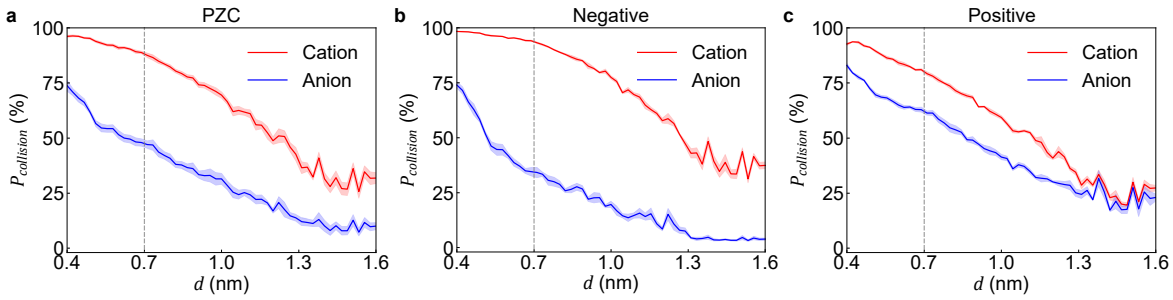

Supplementary Figure 9. The probability of collision between ions and electrodes. **a-c**, The probability of collision between ions and electrode walls at PZC (**a**), in negative (**b**) and positive (**c**) electrodes. The collision occurs when the distance between ions and pore walls is smaller than the sum of their vdW radii.

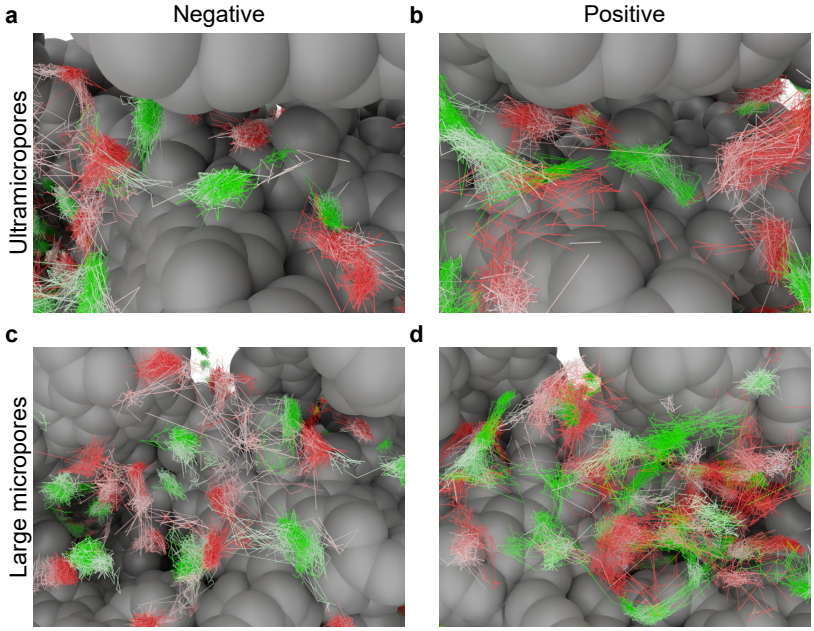

Supplementary Figure 10. The motion path of ions. **a**,**b**, The motion path of ions within ultramicropores of negative (**a**) and positive (**b**) electrodes. **c**,**d**, The motion path of ions within large micropores of negative (**c**) and positive (**d**) electrodes. Lines in red represent trajectories of cations and lines in green represent trajectories of anions. Points or lines in lower saturation (nearly white) mean the trajectory of the early stage.

Section 9. Multi-scale impedance model

The multi-scale impedance model (MIM) is constructed for the carbon supercapacitor cell, considering the real carbon electrode consists of close-packing carbon particles. The electrochemical impedance spectroscopy (EIS) of the whole electrode is determined by the impedance of the inter-particle pores and the impedance of the single particle modelled as FEC. A real particle is considered to consist of multiple FECs in parallel. Each FEC includes the impedance of pores inside the nanoporous carbon particle. For a real particle, the impedance Z_{par} is given by

$$Z_{par} = \frac{Z_{FEC}}{4N_{FEC}}, \tag{S28}$$

where Z_{FEC} refers to the impedance of FEC scaled up from MD simulation to real particle size and N_{FEC} is the number of FEC within a single particle. The contribution of inter-particle pores is the capacitance of the particle's outer surface and the resistance of the large pores formed by inter-particle space. In the model, the inter-particle pores contribute only resistance, since the particle's outer surface is too small which contributes only a little to the overall capacitance. Considering a representative elementary volume (REV) including a single particle and the electrolyte filled in the inter-particle pores (**Supplementary Fig. 11**), the impedance of REVs stacking on the current collector is calculated by:

$$Z_{REV} = \sqrt{R_{out}}\sqrt{Z_{par}}\coth\left[\frac{L_{macro}\sqrt{R_{out}}}{\sqrt{8}r_{par}\sqrt{Z_{par}}}\right], \tag{S29}$$

where r_{par} is the radius of the electrode particle and L_{macro} is the thickness of the real electrode; $R_{out} = \frac{1}{\sqrt{8}r_{par}\sigma_{bulk}\left(1-2\pi/3\sqrt{8}\right)^{5/3}}$ is the resistance of the ions in the inter-particle pores of REV[18], and σ_{bulk} = 1.55 S m^{-1} is the conductivity of bulk electrolyte[19]. The REV is in parallel with each other, and the impedance of the multi-scale impedance model is

$$Z_{elec} = Z_{REV}/N_{REV}, \tag{S30}$$

where the N_{REV} refers to the REV count parallel to the current collector. The

impedance for the whole system Z is then calculated as:

$$Z = 2Z_{elec} + R_{bulk}, \tag{S31}$$

where R_{bulk} is the resistance of the electrolyte reservoir between the two electrodes.

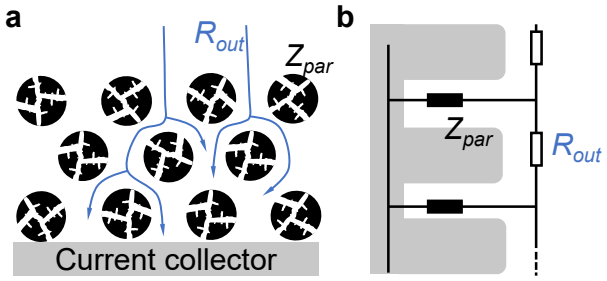

Supplementary Figure 11. The equivalent circuit model for inter-particle pores. a, The ion diffusion in inter-particle pores. **b**, The equivalent circuit for inter-particle ion diffusion within REV.

Supplementary Table 3. The geometry parameters for the MIM

Geometry parameters	Value
L_{macro}	160 μm
r_{par}	2.5 μm
L_{II}	3.1 μm
n_I	1250

Supplementary References

1. Gommes, C. J. Stochastic models of disordered mesoporous materials for small-angle scattering analysis and more. *Microporous and Mesoporous Materials* **257**, 62-78 (2018).
2. Prehal, C. *et al.* Quantification of ion confinement and desolvation in nanoporous carbon supercapacitors with modelling and X-ray scattering. *Nature Energy* **2**, 1-8 (2017).
3. Gommes, C. J. & Roberts, A. P. Structure development of resorcinol-formaldehyde gels: Microphase separation or colloid aggregation. *Physical Review E* **77**, 041409 (2008).
4. Roberts, A. P. Statistical reconstruction of three-dimensional porous media from two-dimensional images. *Physical Review E* **56**, 3203-3212 (1997).
5. Teubner, M. & Strey, R. Origin of the scattering peak in microemulsions. *The Journal of Chemical Physics* **87**, 3195-3200 (1987).
6. Li, T., Senesi, A. J. & Lee, B. Small Angle X-ray Scattering for Nanoparticle Research. *Chemical Reviews* **116**, 11128-11180 (2016).
7. Roberts, A. P. Morphology and thermal conductivity of model organic aerogels. *Physical Review E* **55**, R1286-R1289 (1997).
8. Debye, P., Anderson, H. R. & Brumberger, H. Scattering by an Inhomogeneous Solid. II. The Correlation Function and Its Application. *Journal of Applied Physics* **28**, 679-683 (1957).
9. Gibaud, A., Xue, J. S. & Dahn, J. R. A small angle X-ray scattering study of carbons made from pyrolyzed sugar. *Carbon* **34**, 499-503 (1996).
10. Laudisio, G. *et al.* Carbide-derived carbons: A comparative study of porosity based on small-angle scattering and adsorption isotherms. *Langmuir* **22**, 8945-8950 (2006).
11. Willey, T. M. *et al.* Changes in pore size distribution upon thermal cycling of TATB-based explosives measured by ultra-small angle X-ray scattering. *Propellants Explosives Pyrotechnics* **31**, 466-471 (2006).
12. Pikus, S., Celer, E. B., Jaroniec, M., Solovyov, L. A. & Kozak, M. Studies of intrawall porosity in the hexagonally ordered mesostructures of SBA-15 by small angle X-ray scattering and nitrogen adsorption. *Applied Surface Science* **256**, 5311-5315 (2010).
13. Petzold, A. *et al.* Distribution of Sulfur in Carbon/Sulfur Nanocomposites Analyzed by Small-Angle X-ray Scattering. *Langmuir* **32**, 2780-2786 (2016).
14. Silas, J. A. & Kaler, E. W. Effect of multiple scattering on SANS spectra from bicontinuous microemulsions. *Journal of Colloid and Interface Science* **257**, 291-298 (2003).
15. Agrawal, S., Galmarini, S. & Kröger, M. Voronoi tessellation-based algorithm for determining rigorously defined classical and generalized geometric pore size distributions. *Physical Review E* **107**, 015307 (2023).

16. Merlet, C. *et al.* Highly confined ions store charge more efficiently in supercapacitors. *Nature Communications* **4**, 2701 (2013).
17. Song, H. K., Jung, Y. H., Lee, K. H. & Dao, L. H. Electrochemical impedance spectroscopy of porous electrodes: the effect of pore size distribution. *Electrochimica Acta* **44**, 3513-3519 (1999).
18. Eikerling, M., Kornyshev, A. A. & Lust, E. Optimized Structure of Nanoporous Carbon-Based Double-Layer Capacitors. *Journal of The Electrochemical Society* **152**, E24 (2005).
19. Stoppa, A., Zech, O., Kunz, W. & Buchner, R. The Conductivity of Imidazolium-Based Ionic Liquids from (-35 to 195) °C. A. Variation of Cation's Alkyl Chain. *Journal of Chemical and Engineering Data* **55**, 1768-1773 (2010).